Materials Today • Volume xxx, Number xx • xxxx 202

RESEARCH



Particle tracking microrheology of cancer cells in living subjects

Pei-Hsun Wu^{1,2,*}, Sanjiv Sam Gambhir^{4,5,*}, Christopher M. Hale^{1,2}, Wei-Chiang Chen^{1,2}, Denis Wirtz^{1,2,3,*}, Bryan Ronain Smith^{4,5,6,7,*}

Cumulative evidence shows that microenvironmental conditions play a significant role in the regulation of cell functions, and how cells respond to these conditions are of central importance to regenerative medicine and cancer cell response to therapeutics. Here, we develop a new method to examine cell mechanical properties by analyzing the motion of nanoparticles in living in mice, combining particle tracking with intravital microscopy. This method directly examines the mechanical response of breast carcinoma cells and normal breast epithelial cells under intravital microenvironments. Our results show both carcinoma and normal cells display significantly reduced compliance (less deformability) *in vivo* compared to the same cells cultured in 2D, in both sparse and confluent conditions. While the compliance of the normal cells remains steady over time, the compliance of carcinoma cells decreases further as they form tumor-like architectures. Integrating the cancer cells into spheroids embedded in 3D collagen matrices in part redirected the mechanical response to a state closer to the *in vivo* setting. Overall, our study demonstrates that the microenvironment is a crucial regulator of cell mechanics and the intravital particle tracking method can provide novel insights into the role of cell mechanics *in vivo*.

Introduction

Mounting evidence suggests that changes in cell and nuclear mechanics are hallmarks of many human diseases, particularly metastatic cancer, cardiovascular disease, inflammation, laminopathies, host-microbe interactions in infectious diseases, and frailty in aging [1–6]. In particular, the onset and progression of cancer have long been speculated to be associated with mechanical "softening" of the cytoplasm: Cancer cells are thought to be mechanically more compliant (i.e. softer) than non-cancer cells. However, all these cell-mechanical results have been obtained from *in vitro* culture conditions [7–9]. Cancer cells in solid tumors grow and migrate in a tumor microenvironment that is profoundly more complex than the simplified biochemical and biophysical environment recapitulated with

RESEARCH Original research

¹ Johns Hopkins Physical Sciences-Oncology Center, The Johns Hopkins University, Baltimore, MD 21218, USA

² Department of Chemical and Biomolecular Engineering, The Johns Hopkins University, Baltimore, MD 21218, USA

³ Department of Oncology, Johns Hopkins University School of Medicine, Baltimore, MD 21231, USA

⁴ Department of Radiology, Molecular Imaging Program at Stanford (MIPS), The Bio-X Program, Stanford, CA 94305, USA

⁵ Department of Bioengineering, Department of Materials Science & Engineering, Stanford University, Stanford, CA 94305, USA

⁶ Department of Biomedical Engineering, Michigan State University, East Lansing, MI 48823, USA

⁷ Institute for Quantitative Health Science and Engineering, Michigan State University, East Lansing, MI 48823, USA

Abbreviations: MSD, mean-squared displacement; AFM, atomic force microscopy; SCID, severe combined immunodeficiency; NA, numerical aperture; s.e.m., standard error of the mean.

RESEARCH

susceptible to micro-environmental conditions [11–16]. Direct validation of cell stiffening as a hallmark of tumor progression has been lacking because cells are deeply embedded in a tumor or its surrounding stromal matrix, beyond the direct reach of techniques commonly used to interrogate the mechanics of cells [17], including atomic force microscopy (AFM) [7,17] and micropipette suction [18,19]. These techniques require direct physical contact between the cell surface and the mechanical probe of the instrument (e.g. the cantilever of the AFM, etc.) [8]. Therefore, the mechanical state of cancer cells in solid tumors *in vivo* remains an open question with no tool available to respond.

Cell mechanical properties are tightly regulated by cytoskeletal organization [20-22]. Recent studies have shown that the dynamic profiles of nanoparticles revealed by single-particle tracking (SPT) in living mammalian cells can be influenced by active forces generated by cytoskeletal networks [23-26] as well as the mechanical structure of the cytoskeleton [20-22]. Thus, SPT tracking results reflect the real-time properties of the cytoplasm, which are contributed by both the viscoelastic response of the cytoskeleton [22] and active forces generated by the contractile cytoskeleton. SPT allows for the direct measurement of movements of particles or molecules to determine their transport properties, which provides information on the local environment of the particle. Thus, this approach has been extensively used in culture to monitor dynamic processes of biological systems [27-33]. Intravital microscopy applies lasers and fluorescence imaging to directly visualize biological interactions in small living subjects at high resolution. It has been traditionally used to understand cancer [34,35], immunology [35], neuroscience [35], and more recently the behavior of nanoparticles in living animals [36-39]. Here we show a fully validated framework combining SPT and intravital microscopy to probe cancer cell mechanics in living mice.

Using the proposed intravital SPT method, we studied how cell physical properties are modulated by different microenvironments, including cells in 2D culture dishes, in 3D matrices and within spheroids, and in cells within living mice [11,22,40–43]. We applied our intravital SPT approach to probe for the first time the evolution of the cytoplasmic intracellular properties of breast cancer cells (MDA-MB-231) and non-tumorigenic breast epithelial cells (MCF-10A) grown under intravital microenvironmental conditions over time in living mice. Intravital SPT analysis provides a new platform to directly and dynamically study the material properties of individual live cells in living animals with submicron resolution.

Results

Method for intravital particle tracking at sub-micron resolution Intravital particle tracking was implemented by first surgically implanting an observational window chamber on the dorsal skin of severe combined immunodeficient (SCID) mice (Fig. 1a and Methods) [44]. Fluorescent nanoparticles were ballistically injected into EGFP-transfected MDA-MB-231 human breast cancer cells or MCF-10A human non-tumorigenic mammary epithelial cells, as previously described [21] (Fig. 1b). As opposed to

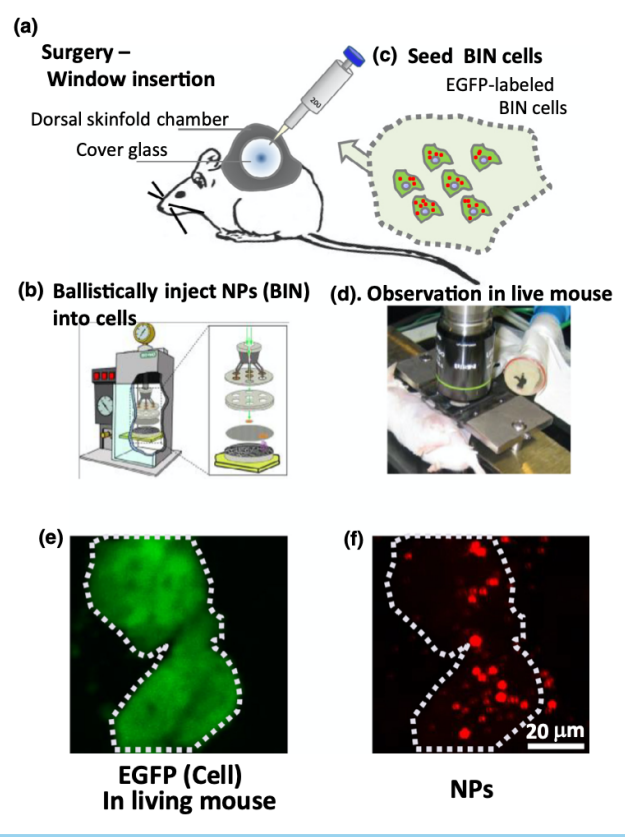


FIGURE 1

Intravital particle tracking microrheology. (a and b) An observation window chamber was surgically implanted into the dorsal skin of a mouse (a). EGFP-transfected human breast cancer (MDA-MB-231) cells were injected with 200 nm diameter fluorescent nanoparticles using a ballistic particle injection system (b). These cells (~250,000) were then implanted (cells, green; nanoparticles, red) directly into the mouse's window chamber (c). The mouse was anesthetized and placed on a custom-made motion stabilization stage for imaging with an intravital microscope for long-term observation. The mouse is imaged on the customized stage of an intravital upright microscope (d). Images of EGFP-labeled cells (green) (e) and fluorescent nanoparticles (red) (f) in the same field-of-view. The white dashed line outlines the cell boundaries; most particles are within cells.

cles [45]. After overnight incubation to allow for recovery and dispersion of the nanoparticles in the cytoplasm, these cells were implanted into the dorsal windows of mice under anesthesia (Fig. 1c). After recovery, the cell physiology was unperturbed by the injected nanoparticles [21]. Mice were motion-stabilized by attachment to a customized microscope stage (Fig. 1d) to image both cells and nanoparticles [46] (Fig. 1e and f). We imaged nanoparticles in 10–25 fields-of-view at each time point for each mouse; nanoparticle displacements were then tracked, which once processed appropriately allowed for computation of mean squared displacements (MSDs) to characterize the materials properties of the cytoplasm. Notably, the injected beads in cells can appear as aggregates and these instances were removed from tracking results to ensure only tracked beads with the appearance of single beads proceeded in the analysis.

Materials Today • Volume xxx, Number xx • xxxx 2020

RESEARCH

probing cells in culture. First, we observed large rhythmic motions (\sim 25–100 nm) caused by the breathing and heartbeat of the mouse, as well as tissue and organ movements. The magnitude of this rhythmic motion masked the small fluctuations of the probing nanoparticles (Fig. 2a–c and Supplementary movie S1). Second, attaining sufficient particle resolution was a major challenge, as intravital microscopy often requires the use of longer working-distance/lower numerical aperture (NA) microscope lenses to probe cells in the tumor and tissues of the mouse (see Methods and supplementary material) [38,47]. Without sufficient temporal resolution, small bead displacements at short time scales cannot be measured.

To address these challenges, we modeled trajectories of cellembedded nanoparticles in living mice (Fig. S1) as the sum of: (i) the small fluctuations of the probing nanoparticles from which rheological properties of the cytoplasm could be extracted; (ii) the large rhythmic movement of the mouse; and (iii) the intrinsic limited spatial resolution of the instrument (called the "static error"; Fig. S2 and Supplementary Materials). MSDs computed from recorded unadulterated trajectories readily show such rhythmic motion ((ii), Fig. 2c). To understand and model the origin of the complex masking "noise" present in both the trajectories (Fig. 2b) and the resulting MSDs (Fig. 2c), we developed a computational model that added static noise and rhythmic motion to the intrinsic (relevant) motion of the beads in the cytoplasm (Fig. S1; see also Supplemental Material). After adding these two distinct contributions, our simulated MSDs recapitulated the MSD profiles observed for nanoparticles in implanted cancer cells in live mice (Fig. S1). This suggests that we correctly identified the origins of the relevant noise sources. We developed a highly integrated procedure to overcome these two sources of noise to create a robust particle tracking method

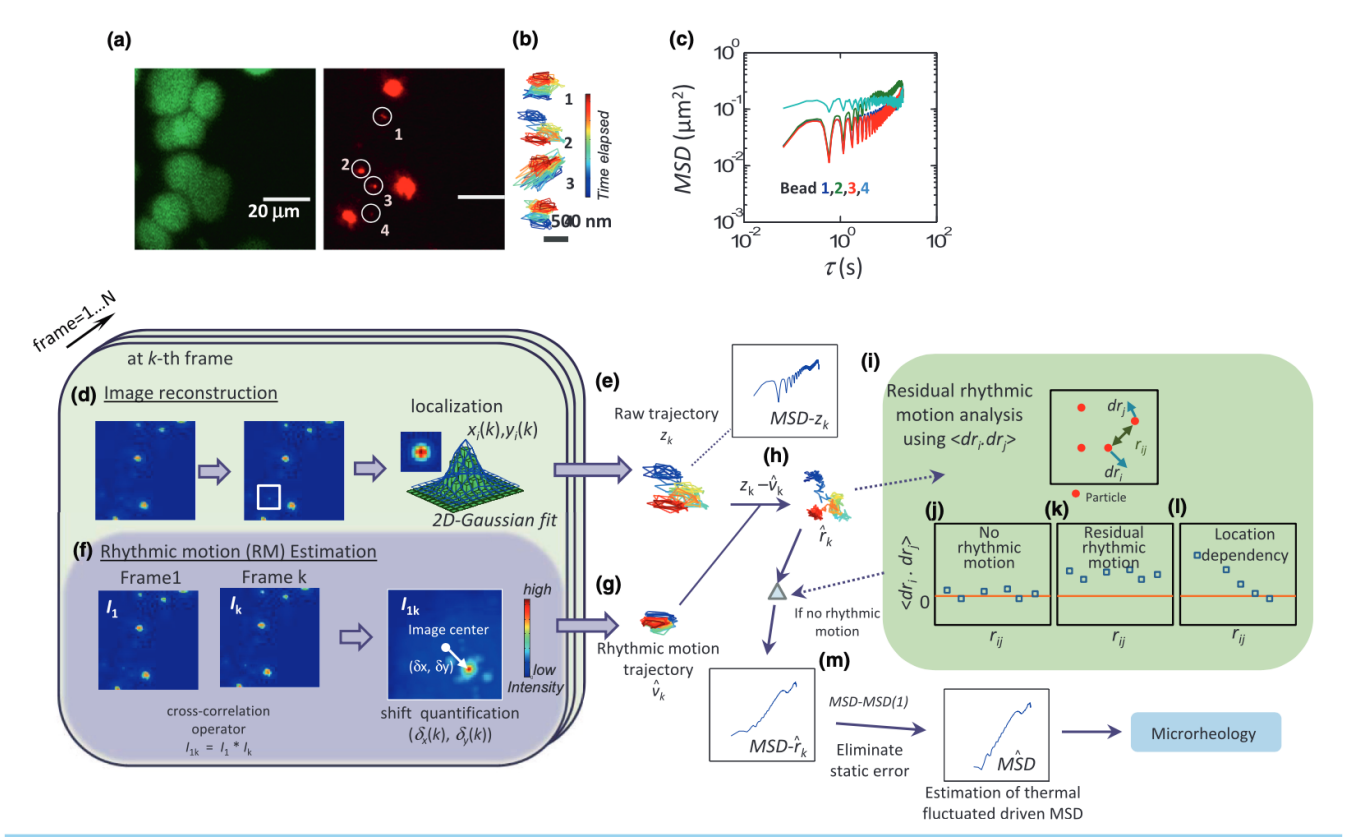


FIGURE 2

Multimodal movements of nanoparticles in intravital particle tracking. (a) EGFP-labeled breast cancer cells and four representative nanoparticles were tracked for 20 s at 15 frames/s (scale bar applied for both images, which are the same field-of-view with separated channels). (b) Unadulterated trajectories of each tracked particle, which are color-coded from blue to red, indicating elapsed time. (c) MSDs were computed from the tracked trajectories of these 4 particles. Large oscillations are readily apparent in all MSDs, likely due to the rhythmic motion induced by the animal. (d-m) Analysis to obtain intracellular mechanical properties of single cancer cells. The image, obtained from high speed scanning confocal microscopy, displays mismatched intensity in between lines. A reconstructed, smoothed image is obtained using only intensity information from odd rows to interpolate intensity distribution across even rows. Sub-pixel localization of the particles in the image is then computed using a 2D Gaussian fit (d). The trajectory of a particle is composed of its locations across entire frames in the video (e). A correlated image (a measure of the "similarity" between two images with regard to different nanoparticle positions offset in x- and y-directions) is obtained by cross-correlating the first and the kth image. The highest intensity in this image is measured using a Gaussian fit and its dislocation from the center of the image gives an estimate of the overall displacement due to the rhythmic motion of the mouse (f-g). The raw trajectories are then calibrated using the estimated trajectories of rhythmic motion to obtain an estimate of the thermal-fluctuation driven trajectory (h). For further

RESEARCH

ARTICLE IN PRESS

Materials Today ◆ Volume xxx, Number xx ◆ xxxx 2020

for living subjects. (See more details and extensive validation for these procedures in Supplementary Materials and Figs. S2–S6).

Three critical steps were taken to overcome the technical challenges caused by SPT in live animals and the use of intravital microscopy (Fig. 2d and e). These steps include: (i) accurate estimation and subtraction of the rhythmic motion of the mouse from the trajectories of the nanoparticles in the field-of-view (Fig. 2f–h, Supplementary Movie S2); (ii) estimation of the residual effects of rhythmic motion on particle trajectories through spatial correlation analysis (Fig. 2i–l); and (iii) subtraction of the intrinsic static error of the intravital microscope (Fig. 2m and S6).

Briefly, for step (i), a k-th cross-correlation image was obtained from the 2D cross-correlation of the first and k-th frames of a video (k ranges from 1 to the last frame N) (light blue panel, Fig. 2f; see more details in Methods). We then automatically determined the location of the highest value of intensity in this correlation image at sub-pixel resolution using a 2D Gaussian fit. The shift vector, determined from this position and the center of the image, represents a shift due to the rhythmic motion of the mice. Conducting this operation from the first to the last frame of the video gave an estimation of the rhythmic motion of the mice (Fig. 2g). Raw trajectories of the nanoparticles were corrected by this calculated shift, which generated revised timedependent coordinates of the nanoparticles (Fig. 2h). In some videos (Supplementary Movie S3), the rhythmic motion did not correspond to rigid-body motion, i.e. the rhythmic motion could not be described by a constant shift vector of the same magnitude and direction for the entire field of view; i.e. these "rhythmic motions" were spatially-dependent (Fig. S5). These spatially-dependent rhythmic motions could, for example, result from rotational movements of mouse tissues/organs in the axial (z-axis) direction and the resulting stress/strain acting on the tissue. Here, we develop a test that identified the correlated movement of nanoparticles in fields-of-view by examining the relationship between the inter-particle distance (R_{ij}) and ensemble-averaged correlation movement, $\langle dr_i \times dr_i \rangle$, between all different paired nanoparticles in a field-of-view. The data fit into three categories (see Schematic in Fig. 2-j-l): the movements of the nanoparticles are uncorrelated (Fig. 2j), all nanoparticles display the same extent of correlation (Fig. 2k), or their degree of correlation decays with their inter-particle distance (Fig. 21). We note that correlation in NP motion within the same cells is likely to be caused by the fact that the cytoplasm could be partially elastic, and is of much smaller magnitude than the spatial correlations caused by the rhythmic motion of the mouse (Fig. S5 and Supplementary movie S2). For each movie, we generated such correlation plots to ensure that there was no significant spatial dependency in correlated movements. Only tracked particles that met both criteria of constant shift vector and zero correlation (e.g., Fig. 2j) were further analyzed to compute the MSD to infer the cytosol mechanical and active cytoskeletal forces.

For step (iii), we determined the intrinsic resolution of the intravital microscope in the absence of the mouse by tracking the spontaneous fluctuations of nanoparticles immobilized on a glass substrate. We first identified the optimal parameters used

to a static error of 3×10^{-3} – 1×10^{-2} µm² (Fig. S2). We found that the MSD profiles of nanoparticles in implanted cancer cells in living mice were flat at short time scales and that at short time scales, MSD values were similar in magnitude to the static error (see above) [21,47,48]. Therefore, we developed a procedure to correct static error by subtracting the static error from raw MSD values. We confirmed the validity of this procedure by both computer simulations and experiments (Figs. S5-S7). The results showed that this analysis provides high accuracy in estimating the ensemble-averaged MSD at intermediate time lag response (\sim 0.6–3 s), when the level of position noise is similar to the static error of our intravital tracking conditions. We established that the minimum measurable MSD value under intravital conditions was approximately $3 \times 10^{-4} \, \mu \text{m}^2$ at a time lag of 0.13 s, which is equivalent to ~ 12 nm resolution in particle movements in the *x*and y-directions.

Real-time intracellular properties of cancer cells in living animals

We tracked the movements of nanoparticles inside living cells after implantation of the cells in the intravital microenvironment for both metastatic breast carcinoma MDA-MB-231 cells and MCF-10A breast epithelial cells. We measured the MSDs of nanoparticles in cells within hours of their initial implantation (referred to as day 0) and at day 2, day 3, day 4, and day 7 post-implantation (Fig. 3a). We found that the ensembleaveraged MSDs for the first four days of data collection were highly similar in magnitude and time-lag dependence (Fig. 3eg), suggesting no change in cell mechanical properties. MSDs displayed an exponent α of the time-lag-dependent MSD close to or slightly larger than one, suggesting that cytoplasmic regions of cells exhibited active forces. As the MDA-MB-231 cells continued to grow in the intravital microenvironment, forming tumor-like clustering architectures, intravital particle tracking revealed a significant decrease in MSD values seven days post-implantation (Fig. 3f) and a reduction in the exponent α (Fig. 3g). These results suggest a reduction of active forces in the cytoskeleton and an increase both in the mechanical stiffness and in the elastic character (as opposed to its viscous character) of the cells as the cells formed a tumor. Importantly, we did not observe significant differences in the MSDs of nanoparticles in cells across different mice (Fig. 3c and d), showing strong measurement consistency.

To further investigate whether these time-dependent properties were a signature of tumorigenic cells, we performed the same intravital measurements using non-tumorigenic MCF-10A breast epithelial cells (Fig. 3h–j). Unlike MDA-MB-231 cells, our results show that nanoparticles in MCF-10A cells grown *in vivo* over 7 days do not exhibit a statistically significant decrease in MSD values and exponents (P > 0.05). Also, as opposed to MDA-MB-231 cells, MCF-10A cells did not display active forces. Overall, MDA-MB-231 cells display higher MSDs and exponent values than MCF-10A cells, indicating that MDA-MB-231 cells have a more compliant cytoplasm than MCF-10A cells [9].

Cell microrheology in vivo vs. in vitro

We next assessed whether microenvironmental factors - such as

Materials Today ● Volume xxx, Number xx ● xxxx 2020

RESEARCH

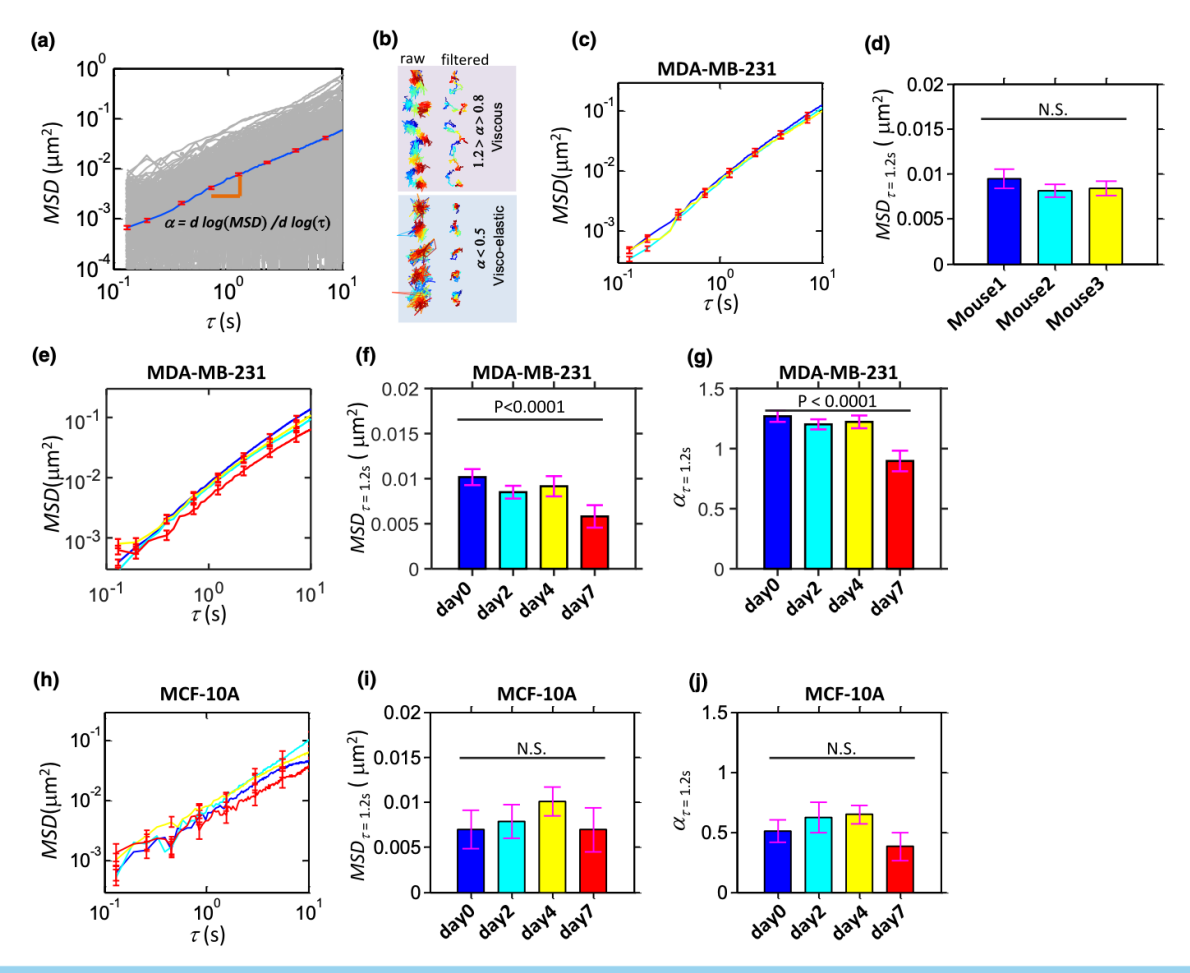


FIGURE 3

Evolution of cancer cell mechanical signature in a living mouse. (a) MSD profiles of observed bead movements in MDA-MB-231 cells across all days (day 0 (N = 302), day 2 (N = 365), day 3 (N = 277), day 4 (N = 137), and day 7 (N = 127)) post-implantation of cells into three different mice. Day 0 represents the measurement of cells within a few hours after implantation. (B) Examples of trajectories from bead movement inside a cell from living mice; two groups of trajectories with distinct exponents α , with the value at τ = 1 shown. The top group of trajectories represents particles undergoing free diffusion where the α value is approximately 1. The bottom group is trajectories with an exponent value below 0.5, which represents nanoparticles within a viscoelastic environment. To reduce the noise in trajectories for better visualization, filtered trajectories were obtained using Kalman filtering. (c and d) Comparison of ensemble-averaged MSD profiles from each mouse (c). Bar graph of MSD values at 1.2 s time lag. No significant difference (p > 0.05) across the three mice is found (d). The sample size of observed beads is 434, 484, and 291 respectively in three mice. (e–g) Ensemble-averaged MSDs obtained at different numbers of days after MDA-MB-231 cells were implanted into the dorsal windows of mice (e). Results show a decrease in MSD value at day 7. The bar graphs of MSD values (f) and exponent α (g) at a time lag of 1.2 s across days post-implantation. A significant difference was found in both MSD values and MSD exponent between different groups. (h–j) Ensemble-averaged MSDs obtained at different numbers of days after MCF-10A cells were implanted in mice (N = 42, 44, 87, and 39 for day 0, day 2, day 4 and day 7) (h). The bar graphs of MSD values (i) and exponent α (j) at a time lag of 1.2 seconds across days post-implantation. No significant difference was found between different groups (P-values were assessed using one-way ANOVA analysis for the exponent α , but the Kruskal-Wallis te

microrheological measurements in cells in live mice with those in several common cell-culture systems for both MDA-MB-231 and MCF-10A cells. Both cell lines were grown on 2D collagen-coated glass-bottom dishes at different densities, either in subconfluent (single cells) or confluent conditions (Fig. 4a). These cells were also seeded in 3D matrices consisting of 1 mg/ml and 2 mg/ml collagen I at low density [49]. The MSD profiles of MDA-MB-231 cells in 2D culture showed that cell density played

conditions than in single cells. The MSDs of nanoparticles in single MDA-MB-231 cells on flat substrates were qualitatively and quantitatively similar to MDA-MB-231 cells grown in 2 mg/ml 3D collagen matrices. However, MDA-MB-231 cells under intravital conditions had significantly lower MSD exponents and MSD values than cells in 2D and 3D culture. We also found significantly lower MSD values for the tumorigenic cells *in vivo* than in all tested culture conditions (Fig. 4c and d).

RESEARCH

Materials Today • Volume xxx, Number xx • xxxx 2020

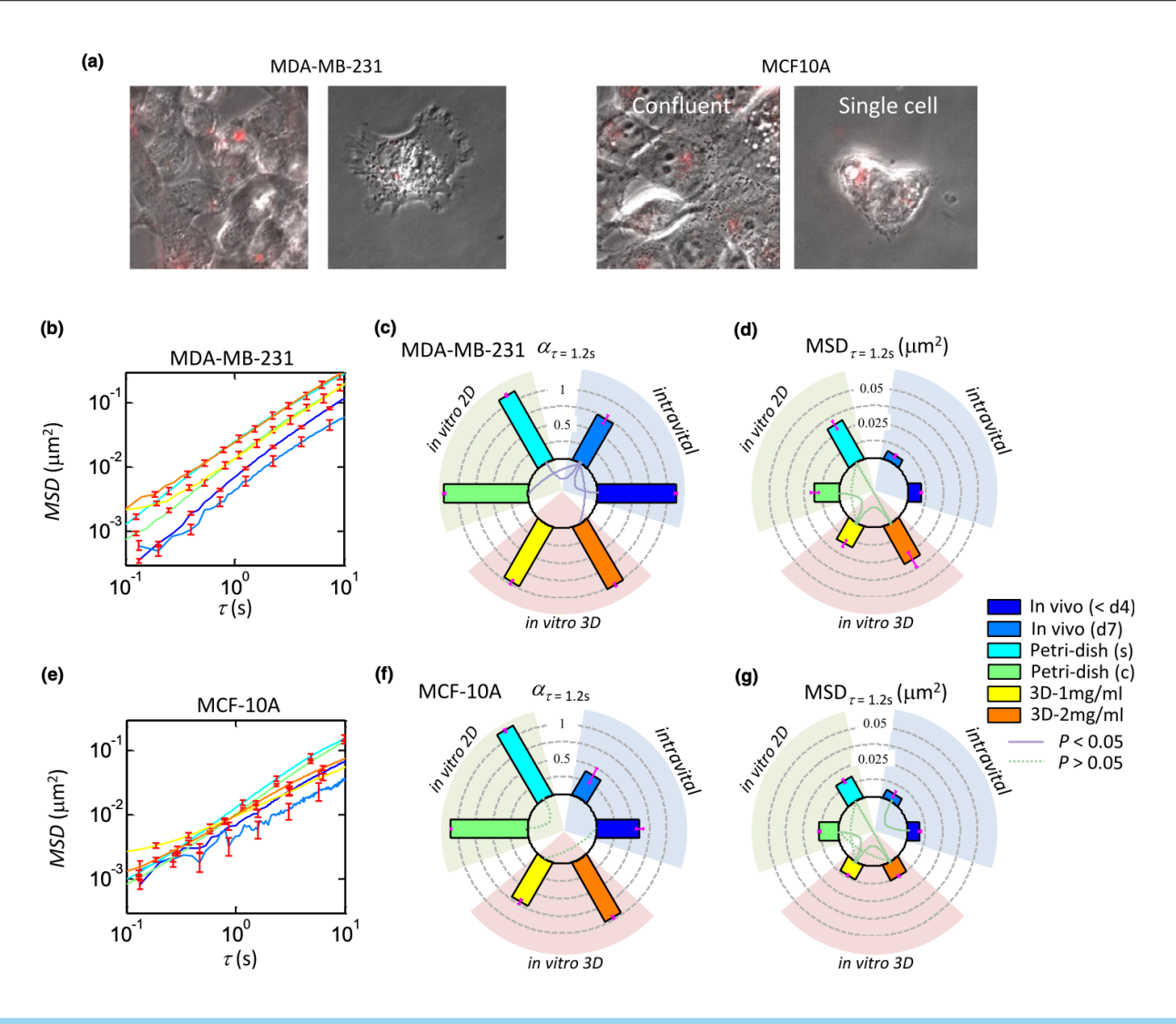


FIGURE 4

Live cell mechanical properties in living mouse vs. in cell culture. (a) Phase images of ballistically injected MDA-MB-231 cells (left) and MCF-10A cells (right) in the single-cell condition and at confluence in culture are overlaid with fluorescent particle images (red). (b) MSD profiles of MDA-MB-231 cells obtained from living subjects (on or before day 4 (N = 1082) and at day 7 (N = 127)) and in culture (single cell (N = 143) and confluent on petri-dish (N = 151); in 1 mg/ml (N = 1082) or 2 mg/ml (N = 71) 3D collagen matrices (N = 126)). (c and d) Bar graphs in a circular layout show MSD exponent (α) and MSD value at a 1.2 s time lag of tumorigenic MDA-MB-231 cells from the six different conditions in (b). Paired cell culture conditions showing a significant difference (P < 0.05) for the MSD exponent are connected by curves in the inner circle of the bar plot. In the MSD bar graph, the connected curves in the inner circle demonstrate the paired conditions that did not show significance (P < 0.05) for visualization purposes (since most of the pairs are significantly different). (e) MSD profiles of MCF-10A cells obtained from these six different conditions. (f and g) Bar graphs in a circular layout show the MSD exponent (α) and the MSD value of non-tumorigenic MCF-10A cells in these six different conditions. Paired cell conditions in culture and in live mice which did not show a significant difference (P < 0.05) for both MSD exponent (α) and MSD values are connected by curves in the inner circle of the bar plot. (N = 173, 39, 149, 614, 79, 116). The significant differences for the exponent α were assessed using one-way ANOVA analyses and Tukey's test. The significant differences for MSD were assessed using the Kruskal-Wallis test and Dunn's test. Each *in vitro* condition shown was replicated twice in the laboratory. Error bars represent the s.e.m.

profiles across the aforementioned very different culture conditions, at least at short time lags (Fig. 4e). The MSD exponent α for MCF-10A cells on a 2D petri-dish, regardless of cell density, was significantly higher ($\alpha > 1$) than measured in intravital conditions and in 3D collagen I matrices (P < 0.05, Fig. 4f). Moreover, cells in 2D or 3D cultures were significantly different from cells *in vivo*, but unlike MDA-MB-231 cells, the microme-

for both types of cells on dishes, which suggests that 2D culture conditions may induce more active cellular forces. MSDs of nanoparticles in MDA-MB-231 cells under intravital conditions progressively resembled the MSDs of nanoparticles in MDA-MB-231 cells in culture conditions as a function of increasing cell-cell contacts on a petri dish or embedded within 1 mg/ml collagen I matrices. However, MCF-10A cells in 3D 1 mg/ml col-

Materials Today • Volume xxx, Number xx • xxxx 2020

RESEARCH

properties and active forces in the cytoplasm are sensitive to the local cell microenvironment including cell–cell contacts, dimensionality, and collagen density.

A recent study suggests that cell density (i.e. the number of cells per unit volume) can trigger changes in the physiological state of cells through IL6/IL8/JNK/STAT3 signaling [49]. Hence, we further compared the MSDs of nanoparticles in MDA-MB-231 cells at low (~ 1000 cells/ μL) and high cell density $(\sim 100,000 \text{ cells/}\mu\text{L})$ within spheroids in 1 mg/ml and 2 mg/ml collagen I 3D matrices (Fig. 5a). Our results show that cell density had little effect on nanoparticle MSDs in both 1 mg/ml and 2 mg/ml 3D collagen I matrices. However, relative to the cells in low density, the exponent α showed a 25% increase for MDA-MB-231 cells in spheroids in 1 mg/ml collagen matrices; conversely, the MSD value at a time lag of 1.2 s shows a \sim 2.5fold decrease for cells in spheroids in 2 mg/ml collagen matrices (Fig. 5b-e). We found that cells in spheroids in 2 mg/ml collagen matrices have the lowest MSD value among all in vitro culture conditions, with high similarity to the value measured in

intravital conditions (Fig. 5f). Notably, across all conditions, our results indicate that tumor cells were stiffest in the living animal, which are displayed in Fig. 5f, in comparison to all 3D culture conditions. Our results indicate that the 2 mg/ml collagen gel setting in spheroids reprograms the mechanics of cells toward those in living animals.

Discussion

We have introduced a new method to track nanoparticles in cells implanted in living subjects based on intravital microscopy, allowing us to monitor the motion of nanoparticles with both high temporal (<100 ms) and spatial resolutions (<15 nm). This method has been fully validated by identifying and computationally eliminating the sources of noise and rhythmic motion. *In vivo* measurements were compared to *in vitro* measurements in various 2D and 3D cell culture settings.

Conventional wisdom holds that the cytoskeleton organization and associated mechanical properties of cells in living

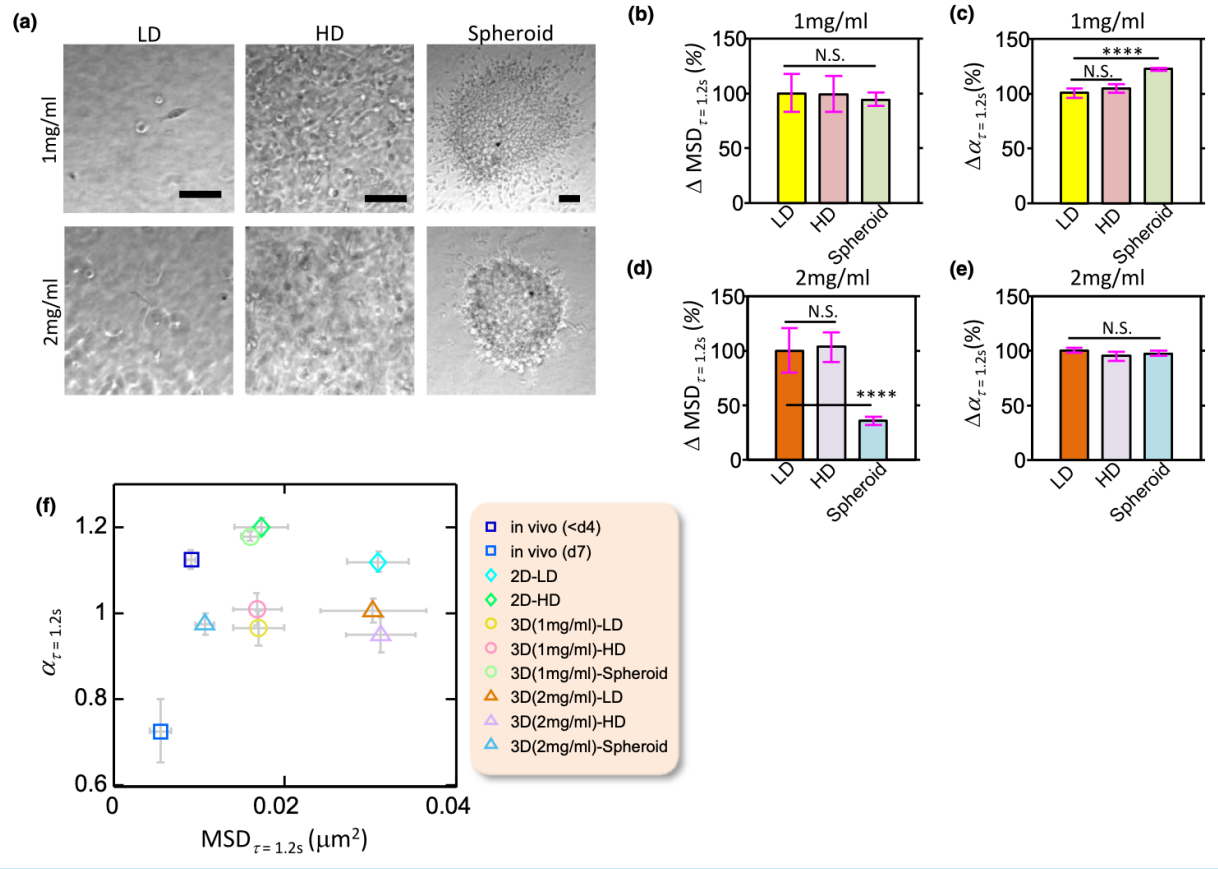


FIGURE 5

Live cell mechanical properties in 3D tumor spheroid. (a) Phase images of ballistically-injected MDA-MB-231 cells in 1 mg/ml (top) and 2 mg/ml (bottom) 3D collagen matrices with low seeding density (LD) (left), high seeding density (middle), and in spheroids. Scale bars represent 100 μ m. (b–e) Bar graphs show the effects of increasing cell–cell contacts on MSD exponent (α) and MSD value from low-density seeding in 3D 1 mg/ml collagen matrices (b and c) and 2 mg/ml collagen matrices (d and e) by seeding with high cell densities or forming spheroids. The MSD exponent and value were extracted at a time lag of 1.2 s. The MSD value decreases significantly for cells in spheroids in 2 mg/ml collagen matrices, while the MSD exponent increases significantly for cells in 3D 4 mg/ml collagen matrices.

Materials Today • Volume xxx, Number xx • xxxx 2020

animals are substantially different than those in cell culture [11]. Our results readily show that the mechanical profiles of cells in culture are more compliant than cells under intravital conditions for both MDA-MB-231 and MCF-10A cells within the timeframes of our measurements from a few hours (day 0) to 7 days after implantation (Figs. 3 and 4). Experiments in 2D and 3D culture have highlighted mechanical differences as high as an order of magnitude [49], and it is natural to expect that these differences might be magnified when studied in live animals [11,40,50]. Our results in living mice are intriguing in this context. First, the results show surprisingly large differences in MSDs between tumor cells grown to confluence and sub-confluence in 2D culture, but not for non-tumorigenic cells (Fig. 4). This is particularly interesting since cell confluence affects cell-cell contacts, which increase vinculin phosphorylation and may thereby increase intracellular stiffness [51]. Second, we were surprised to find that dispersed 2D cultured tumor (MDA-MB-231) cells display MSD profiles similar to cells in 3D culture at both collagen densities tested, yet different from that in live mice (Fig. 4d). In culture, experiments are often performed on individual cells (e.g., using AFM, resonators, pillars) [52–54], so cell–cell contacts and their effects are not assessed. Our data suggest that, at least for tumorigenic MDA-MB-231 cells, increasing cell-cell contacts regulates intracellular properties more than the substrate properties [55] This is likely due at least in part to the fact that mechanical tension on cadherins (which mediate cell-cell interactions), but not integrins (which mediate cell-matrix interactions), induces vinculin phosphorylation and leads to cell stiffening [51]. Indeed, solid tumor formation is driven in part by the upregulation of cell adhesion molecule PVRL4 (poliovirusreceptor-like 4) which promotes cell-cell attachments and anchorage-independence. Additionally, an increase in cell density may cause a reduction in cell volume, leading to molecular crowding and hence increased cellular stiffness [56]. These results could explain our finding that individual tumor cells undergo stiffening as they form a tumor by day 7, since solid tumors up-regulate molecules that drive cell-cell connections [57] and hence result in stiffer cells [51]. Thus, likely the most important parameter from living subjects to mimic in culture may be proximity to other cells rather than the substrate used at least in tumor cells.

Further experiments are required to determine the underlying molecular mechanisms as well as whether the differences may be due to cell line tumorigenicity or simply due to differences between cell lines. Preliminary experiments on cell molecular markers suggest that EMT/MET (epithelial–mesenchymal transition, mesenchymal–epithelial transition) processes do not play a major role (data not shown). In fact, based on the similarities in the significance between the two cell lines' *in vitro* conditions, it is likely that the stiffening of MDA-MB-231 tumor cells on day 7 is due to tumor formation. Furthermore, our results suggest that, based on the real-time cytoskeletal properties, one could better model MDA-MB-231 cells in living subjects with a spheroid assay at 2 mg/ml collagen density (Fig. 5d–f), given that the MSD value is similar, though alpha is not.

While biochemical aspects of tumor formation and progres-

Though actual tumor progression in humans could be different from that in mice, the translation of particle tracking microrheology into living animals provides direct insight to questions and will allow direct comparison to physical models [43]. One might expect that given the diverse interactions of cells with their microenvironment, tumor cells might respond mechanically day-to-day as they form a solid tumor. Intriguingly, our results suggest that on average both cell lines tested are mechanically similar from ~1 to 2 h post-implantation through 4-days post-implantation. Then on day seven, we observe significant stiffening in the tumorigenic cell line (Fig. 4b and d) compared with earlier days. These mechanical variations coincide with the onset of tumor angiogenesis on day 6-7 after tumor inoculation [59], and combined with the observed coalescence of tumor cells into a "tumor-like structure" as visualized by intravital imaging, are likely indicative of the formation of a solid tumor [60,61]. Thus, speculatively, the modulation of the mechanical properties of tumor cells upon solid tumor initiation may reflect a shift in the "objectives" of the tumor's constituent cells: while the cells were in the process of forming tumor structures in the early stage, motility was a preferred phenotypic trait. Yet once the cells reached a critical point of tumor formation (exemplified by the release of angiogenic factors forming vessels), they may have entered a different state in which motility decreased in importance in lieu of increased focus upon proliferation and further establishment of the tumor. No significant MSD changes were observed in non-tumor forming MCF-10A cells in the same day 7 time frame. Further experiments, including measurements beyond seven days in live mice, will be required to verify if the changes in MDA-MB-231 cells are meaningful and to better understand this phenomenon.

The mechanical properties of cells measured by particle tracking microrheology can display substantially different values from those measured by other techniques such as atomic force microscopy. Recently, we extensively compared mechanical measurements on MCF-7 cells, obtained through some of the most widely used methods for cell mechanics: atomic force microscopy, magnetic twisting cytometry, particle tracking microrheology, parallel-plate rheometry, cell monolayer rheology, and optical stretching [8]. The results highlight that elastic and viscous moduli of the same cells can vary more than 100-fold and 1000-fold, respectively, across different measurement types. For instance, particle tracking microrheology can quantify elastic moduli at up to 100-fold lower values than other methods, aside from optical stretching, measured at 30 Hz. The substantial differences in measured elastic moduli across various mechanical measurement methods are attributed to the diverse levels of applied mechanical stress, the rate of deformation, the geometry of the probe, the precise location probed in the cell, and the extracellular microenvironment among the different methods.

This work translates SPT imaging technology from cell culture to live subjects, allowing us to extract and quantify, for the first time, the dynamic intracellular properties of individual implanted cells in live animals through high-resolution particle tracking.

We note this technique does not measure all aspects of cellu-

Materials Today • Volume xxx, Number xx • xxxx 2020

RESEARCH

lation into living animals. Furthermore, in its current iteration, the technique allows for tracking of dynamic properties only of implanted cells; however, by using ballistic injection in living subjects (previously used for gene delivery) [62], it may eventually be possible to similarly study native cells, potentially even for clinical applications [63].

Our new method could be used in the future to precisely monitor the intracellular movements of drug and gene delivery vehicles in living subjects and to extract non-averaged transport properties of these nanoparticles. Alternatively, it can be used to validate that particular culture conditions sufficiently mimic conditions in living subjects for further research. Most importantly, the technique allows the study of cell dynamics in living subjects, particularly during time-varying biological and disease processes.

Methods

Intravital microscopy for particle tracking

Cells were ballistically injected with red fluorescent 200-nm diameter fluorescent polystyrene particles (Invitrogen). We also note that nanoparticles remained inside cultured cells for at least 10 days: we could measure the microrheological properties of the same tumor cells in culture for 10 days after injection in cell culture, through the repeated dilution of the nanoparticles during each cell division [21,64].

A titanium window chamber (APJ Trading, Ventura, CA) was surgically implanted onto the dorsum of retired male breeder 9–12 month old C.B-17 SCID mice (n = 3 per group, used based on our estimates for numbers of cells available to image and our experience in imaging animals) three days before implantation of the tumor cells [44]. No randomization nor blinding was used in this study. On the third day after surgery, ~250,000 cells containing the fluorescent particles were implanted beneath the window. An Olympus IV-100 intravital microscope with 20× Olympus air objectives was used to dynamically image the particles and tumor cells within a living mouse over 1 week (Fig. 1). Video-based particle tracking techniques described below were then used to analyze the movements of the cell-embedded particles at multiple timepoints over a period of seven days. In order to track the random, thermally-driven motion of the particles at sufficiently high speed, a bidirectional scan was used to scan a small region of interest corresponding to a size of 256 × 256 pixels (pixel size, 299 nm) to achieve 15 frames/s temporal resolution. All mouse experiments were carried out under Stanford University Institutional Animal Care and Use Committee (IACUC) Approval.

Image processing and particle tracking algorithm

High-magnification images obtained in the bi-directional scanning mode displayed an interlinear artifact related to spatial scanhead offset (Fig. 3a). This image artifact generated difficulties in the automatic identification and location of the particles in the images. Because this issue was apparently due to a small spatial offset of the scanhead as it traces the sample bi-directionally, we collected intensity profiles from every odd line (equivalent to using every even line) and used a spline interpolation method to

dependent particle locations through a customized code developed in MATLAB (Mathworks). We tested different algorithms and different tracking parameters to identify the method of particle tracking and associated parameters that produced the best spatial resolution for bead tracking (i.e. the smallest value of the MSD when beads were fixed, Fig. S3) in live subjects. We found that the Gaussian fit described in Wu et al. [21] with a fitting window size of 3 by 3 gave the highest spatial resolution.

We implemented computation of the time-dependent positions of the nanoparticles using the procedure developed in our previous work for particle tracking in culture [21]. The location of the same particles in a subsequent frame was then searched based on the nearest locations. Particle trajectories from experimental observation, z_k , could then be obtained.

Rhythmic motion estimation, elimination and validations

Here we describe how we estimated the experimentally observed rhythmic motion in NP trajectories collected in cancer cells in a tumor in a live mouse. A cross-correlated image for the k-th frame, $I_{CC,k}$, is obtained from cross-correlation of the k-th frame, I_k , and the first frame, I_1 , of a tracking N-frame video, i.e.

$$I_{CC,k}(x,y) = \sum_{m=1}^{M} \sum_{n=1}^{N} I_k(m,n) \cdot I_1(m+x,n+y), \tag{1}$$

where $0 \le x < 2 \cdot M - 1$ and $0 \le y < 2 \cdot N - 1$ and M, N are the dimensions of the images in the videos. The vector from the location of the highest intensity value in the cross-correlated image $I_{CC,k}$ to the center location of $I_{CC,k}$ gives the estimation for the shift of field-of-view between the k-th frame and the first frame and was determined with sub-pixel resolution by applying a 2D Gaussian fit to a 3×3 pixel window region around the pixel having the highest correlation value. Going through this process, from frame 1 to frame N, we then obtained the frame-dependent field trajectories of the rhythmic motion, $\widehat{\nu}_k$ (Fig. 3d) where the hat symbol represents the estimated value. We obtained trajectories corrected for rhythmic motion, $\widehat{\tau}_k$, by subtracting $\widehat{\nu}_k$ from the raw trajectories, \widehat{z}_k .

To further validate that these trajectories, \hat{r}_k , were free of rhythmic motion, we quantified the correlative movement in the same field-of-view between different pairs of tracked particles. The correlative movement among a pair of particles i and j, $d\mathbf{r}_{ij}$, is determined by the ensemble average product of these two particle displacements, i.e.,

$$dr_{ij} = \langle dr_i \cdot dr_j \rangle.$$
(2)

Here $dr_i = r_i(k + \tau) - r_i(k)$, $dr_j = r_j(k + \tau) - r_j(k)$, where $r_i(k), r_j(k)$ are the trajectories of particles i and j. Trajectories properly corrected for mouse rhythmic motion should have negligible correlation of movement and hence dr_{ij} should approximately be zero regardless of the distance R_{ij} between particles i and j. Therefore, a linear fit was implemented to evaluate the relationship between R_{ij} and dr_{ij} and we only selected MSDs from fields of tracking in which there was no relationship between dr_{ij} and R_{ij} (i.e., R-squared value <0.2) for all different paired particles. This procedure limited the total number of particles tracked, but is essential

RESEARCH

Estimation of mean squared displacement in intravital setting. The mean-square displacement (MSD) of a bead is computed from the lateral trajectory of that bead. Individual time-averaged MSDs are expressed by the formula,

$$\left\langle M\hat{S}D(\tau)\right\rangle = \left\langle \left(\hat{x}(t+\tau) - \hat{x}(t)\right)^2 + \left(\hat{y}(t+\tau) - \hat{y}(t)\right)\right\rangle^2. \tag{3}$$

Here x(t) and y(t) represent the trajectories of an NP in the x and y directions, t is the elapsed time, τ is the time lag, and the brackets represent time averaging.

Due to the observation noise, this $\langle M\widehat{S}D(\tau)\rangle$ was convolved with a static error [48,65], and can be described by the following relation:

$$\left\langle \hat{MSD}(\tau) \right\rangle = \left\langle \hat{MSD}(\tau) \right\rangle_{NF} + 2\sigma_N^2.$$
 (4)

Here $\langle MSD(\tau)\rangle_{NF}$ is the noise-free MSD and $2\sigma_N^2$ is the static error. An MSD estimated from tracked particles in living subjects is dominated by static error at short time lags (s). In general, this observation noise is Gaussian white noise, and hence σ_N^2 can be considered a τ -independent constant. Therefore, σ_N^2 can be approximated by $\left\langle M\hat{S}D(\tau=\tau_{min})\right\rangle$. Hence, a noise-free MSD, $\left\langle M\hat{S}D(\tau)\right\rangle_{NF}$, can be obtained by subtracting $\widehat{\sigma}_N^2$ from $\left\langle M\hat{S}D(\tau)\right\rangle$, i.e.,

$$\left\langle M\hat{S}D(\tau)\right\rangle_{NF} = \left\langle M\hat{S}D(\tau)\right\rangle - \hat{\sigma}_{N}^{2}
= \left\langle M\hat{S}D(\tau)\right\rangle - \left\langle M\hat{S}D(\tau = \tau_{\min})\right\rangle$$
(5)

We used MSD profiles of individual beads to rule out the noneligible beads. This MSD correction procedure is valid only for beads displaying static error-dominant MSD profiles at a short time lag. Since static error-dominant raw MSD profiles at short time lag display time lag-independent MSD values, we only used raw MSD data for which exponents at short time lag (0.12 ms) are less than 0.2 for further analysis.

Code availability

The MATLAB code for tracking analysis is available upon request.

Cell culture and ballistic particle injection

EGFP-tagged human breast cancer cells (MDA-MB-231) (a generous gift from Dr. Owen McCarty, Oregon Heath and Science University) were cultured in DMEM supplemented with 10% fetal bovine serum (Hyclone, Logan, UT), 100 IU/ml penicillin, and 100 µg/ml streptomycin and maintained at 37 °C in a humidified, 5% CO₂ environment. EGFP-tagged nontransformed human breast epithelial cells (MCF-10A) were cultured in 5% horse serum supplemented with 20 ng/ml hEGF, 10 μg/ml insulin, 100 ng/ml cholera toxin, and 0.5 µg/ml hydrocortisone [66]. Cells were passaged every 3–4 days and seeded at 1×10^4 cells/ml onto 10-cm cell culture dishes. For ballistic particle injection, both MDA-MB-231 and MCF-10A cells were plated on 100-mm cell culture dishes and subjected to ballistic injection carboxylated polystyrene fluorophore-laden 200-nm nanospheres (Invitrogen) using a Biolistic PDS-1000/HE nanoparticles previously dialyzed in ethanol were coated on macrocarriers and allowed to dry for 2 h. Macrocarriers were loaded into a hepta-adaptor and bombardment was carried out using 900 psi and 1100 psi rupture discs for MDA-MB-231 and MCF-10A, respectively. After injection, cells were washed three times in PBS and subsequently incubated in regular growth media. For the cell culture study, cells were seeded either on collagen-coated glass substrates or in 1 mg/ml or 2 mg/ml collagen I matrix [12,16] overnight before imaging. To prepare the 3D collagen I culture system, cells suspended in a 1:1 (vol/vol) ratio of cell culture medium and reconstitution buffer (0.2 M Hepes (Sigma-Aldrich, St. Louis, MO), 0.26 M NaHCO3 (Sigma-Aldrich), and water as solvent) were mixed with the appropriate volume of soluble rat-tail collagen I (Corning, Glendale, AZ) to obtain the desired target collagen concentration. A calculated amount of 1 M NaOH was added quickly, and the final solution was mixed well to bring the pH to \sim 7. The cell suspension was added to a 24-well coverslip-bottom cell-culture dish and immediately transferred to an incubator maintained at 37 °C to allow polymerization. To achieve low and high cell densities, 10,000 and 550,000 cells were seeded respectively within collagen gel. Multicellular spheroids were prepared by following the protocol used in Mason et. al. [67]. In brief, cells were suspended in their regular medium supplemented with 25% Methocult and seeded at 5000 cells per well in non-adherent 96-well round-bottom plates. Plates were centrifuged at 1100 rpm for 5 min and cultured in incubators for 2 days to form spheroids. Spheroids in different wells were then harvested and embedded within collagen matrices. For part of the intravital study, the day after injection, bombarded cells were frozen down in cryovials, stored in liquid nitrogen tanks, and the cell lines were re-established in a distant facility where the intravital microscope was located. Following thaw, only one passage was allowed before tracking to minimize the loss of injected beads upon cell division.

Microscopy for particle tracking in 2D and 3D cell culture

A Nikon TE 2000-E inverted microscope equipped with a Luca-R EMCCD camera (Andor, South Windsor, CT) was used to acquire the time-course images of fluorescent particles for each sample. Ultraviolet-visible light from X-Cite 120Q (EXFO, Mississauga, Ontario, Canada) incorporated with a G-2E/C filter (528-553:590-630 excitation/emission, Nikon) was used to excite the fluorescent particles. For tracking particles in 2D and 3D cell culture, a 60× oil-immersion, N.A. 1.4 objective lens (Nikon, Melville, NY) and a 40× water-immersion, N.A. 1.15 long working distance objective lens (Nikon) were used separately. For optimal temporal- and spatial-resolution in tracking, 2-by-2 binning was imposed to scan a field of view of 300 × 300 pixels to enhance the signal/noise ratio (SNR) in reading pixels [47]. As a result, the pixel size for 2D and 3D is 260 nm and 400 nm and temporal resolution for 2D and 3D tracking systems is 30.9 and 21.5 fps with an exposure time of 6 ms and 20 ms. The long exposure time for the 3D tracking system was used for the admission of better photon signals in pixels due to use of a lower N.A. objective lens. In each tracking run, a stack of more than 580

Materials Today • Volume xxx, Number xx • xxxx 2020

RESEARCH

Simulation of experimentally-measured nanoparticle trajectories in living mice

To understand the origin of the apparent rhythmic motion in the measured unadulterated trajectories of nanoparticles embedded in cells in living subjects, we conducted computer simulations of nanoparticles movements. These movements of nanoparticles were assumed to contain the sum of an underlying small-magnitude Brownian component, large-magnitude rhythmic motion and large-magnitude steady movements of the mouse, and noise due to the limited resolution of the intravital microscope. Hence, the position vector of each particle, from time k-1 to time k, was described by the following process:

$$x_k = x_{k-1} + \delta_{BR} + \delta_{VB} \tag{6}$$

Here x_k is the lateral position vector describing the NP positions in the x- and y-directions at time k; δ_{BR} and δ_{VB} represent the displacements resulting from the Brownian motion of the nanoparticles and from the rhythmic motion of the mouse. The displacement δ_{BR} is statistically determined by $\delta_{BR} N(0, \sigma_{BR}^2)$, where $N(0, \sigma_{BR}^2)$ represents the distribution of a random variable of zero mean and variance equal to σ_{BR}^2 . The rhythmic motion component of NP movements δ_{VB} was described by the following expression:

$$\delta_{VB}(k) = A \cdot \sin(\omega k) + \nu_0. \tag{7}$$

Here A and ω represent the amplitude and frequency of oscillation, respectively, and v_0 is the constant shift due to the movements of the mouse. Hence, the component of the particle trajectory due to the rhythmic motion of the mouse, v_k , can be reconstructed by

$$\nu_k = \nu_{k-1} + \delta_{VB}(k). \tag{8}$$

In addition, the component of the particle trajectory due to Brownian motion, r_k , can be reconstituted using

$$r_k = r_{k-1} + \delta_{BR}(k). \tag{9}$$

The experimentally observed positions, z_k , are equal to the true locations plus an observation noise, ε_x , which can be formulated as

$$z_k = x_k + \varepsilon_x, \tag{10}$$

where $\varepsilon_x N(0, \sigma_N^2)$ and σ_N^2 is the magnitude of the observation noise. The results of the simulations described above are shown in Fig. 2.

CRediT authorship contribution statement

Pei-Hsun Wu: Conceptualization, Methodology, Software, Investigation, Formal analysis, Resources, Visualization, Writing - original draft, Writing - review & editing. **Sanjiv Sam Gambhir:** Supervision, Funding acquisition, Writing - original draft. **Christopher M. Hale:** Conceptualization, Investigation. **Wei-Chiang Chen:** Investigation. **Denis Wirtz:** Conceptualization, Supervision, Funding acquisition, Writing - original draft, Writing - review & editing. **Bryan Ronain Smith:** Con-

Acknowledgements

We thank Prof. Virginia Walbot for access to a Biolistic PDS-1000/HE and Dr. Yiider Tseng for fruitful discussions. We also gratefully acknowledge the following sources of funding: K99CA160764 (BRS), NCI PSOC U54CA143907 pilot project (BRS, CMH), NCI CCNE-TR U54 CA119367 (SSG), NCI CCNE-T U54CA151459 (SSG), NCI ICMIC P50CA114747 (SSG), Canary Foundation (SSG), NIGMS R01GM084204 (DW), NCI PSOC U54CA143868 (DW), NCI R01CA174388 (DW), and 12POST12050638 (P.H.W.).

Author contributions

B.R.S., C.M.H., P.H.W., S.S.G., and D.W. designed the experiments. B.R.S., P.H.W., C.M.H. and W.C.C. collected the data; P. H.W. developed the analytical tools and analyzed the data. P. H.W composed the figures and wrote the supplemental material and supplemental figures. P.H.W, B.R.S, and D.W. wrote the manuscript. S.S.G. edited the manuscript.

Appendix A. Supplementary data

Supplementary data to this article can be found online at https://doi.org/10.1016/j.mattod.2020.03.021.

References

- [1] J. Guck et al., Biophys. J. 88 (2005) 3689-3698.
- [2] D. Wirtz, K. Konstantopoulos, P.C. Searson, Nat. Rev. Cancer 11 (2011) 512–522.
- [3] J. Lammerding et al., J. Clin. Invest. 113 (2004) 370–378.
- [4] J.M. Phillip et al., Annu. Rev. Biomed. Eng. 17 (2015) 113-141.
- [5] N. Bufi et al., Biophys. J. 108 (2015) 2181-2190.
- [6] M.J. Harris, D. Wirtz, P.H. Wu, Semin. Cell Dev. Biol. (2018).
- [7] S.E. Cross et al., Nat. Nanotechnol. 2 (2007) 780-783.
- [8] P.H. Wu et al., Nat. Methods 15 (2018) 491–498.
- [9] D.B. Agus et al., Sci. Rep. 3 (2013) 1449.
- [10] B.R. Daniels, B.C. Masi, D. Wirtz, Biophys. J. 90 (2006) 4712-4719.
- [11] F. Pampaloni, E.G. Reynaud, E.H. Stelzer, Nat. Rev. Mol. Cell Biol. 8 (2007) 839–845.
- [12] S.I. Fraley et al., Nat. Cell Biol. 12 (2010) 598-604.
- [13] F. Wang et al., PNAS 95 (1998) 14821-14826.
- [14] C. Li et al., Cancer Res. 66 (2006) 1990–1999.
- [15] K.M. Yamada, E. Cukierman, Cell 130 (2007) 601-610.
- [16] P.H. Wu et al., PNAS 111 (2014) 3949-3954.
- [17] G. Bao, S. Suresh, Nat. Mater. 2 (2003) 715-725.
- [18] R.P. Rand, A.C. Burton, Biophys. J. 4 (1964) 115.
- [19] N. Mohandas, E. Evans, Annu. Rev. Biophys. Biomed. 23 (1994) 787–818.
- [20] J. Apgar et al., Biophys. J. 79 (2000) 1095-1106.
- [21] P.H. Wu et al., Nat. Protoc. 7 (2012) 155–170.
- [22] D. Wirtz, Annu. Rev. Biophys. 38 (2009) 301-326.
- [23] M. Guo et al., Cell 158 (2014) 822-832.
- [24] D. Mizuno et al., Science 315 (2007) 370-373.
- [25] A.W.C. Lau et al., Phys. Rev. Lett. 91 (2003).
- [26] C. Wilhelm, Phys. Rev. Lett. 101 (2008).
- [27] H. Kato, Nat. Nanotechnol. 6 (2011) 139–140.[28] M. Platani et al., Nat. Cell Biol. 4 (2002) 502–508.
- [29] M.J. Saxton, K. Jacobson, Annu. Rev. Biophys. Biomed. 26 (1997) 373–399.
- [30] B. Brandenburg, X.W. Zhuang, Nat. Rev. Microbiol. 5 (2007) 197–208.
- [31] H. Bannai et al., Neuron 62 (2009) 670–682.
- [32] C. Bats, L. Groc, D. Choquet, Neuron 53 (2007) 719–734.
- [33] M. Dahan et al., Science 302 (2003) 442–445.
- [34] D. Fukumura et al., Microcirculation 17 (2010) 206-225.
- [35] M.J. Pittet, R. Weissleder, Cell 147 (2011) 983-991.
- [36] B.R. Smith et al., Nano Lett. 8 (2008) 2599–2606.
- [37] B.R. Smith et al., Small 6 (2010) 2222-2229.

RESEARCH

Materials Today • Volume xxx, Number xx • xxxx 2020

- [41] D.E. Ingber, Semin. Cancer Biol. 18 (2008) 356–364.
- [42] S. Huang, D.E. Ingber, Cancer Cell 8 (2005) 175-176.
- [43] P. Katira, M.H. Zaman, R.T. Bonnecaze, Phys. Rev. Lett. 108 (2012) 028103.
- [44] B.R. Smith et al., Nano Today 8 (2013).
- [45] C.M. Hale, S.X. Sun, D. Wirtz, PLoS ONE 4 (2009) e7054.
- [46] B.R. Smith et al., Nat. Nanotechnol. (2014).
- [47] P.H. Wu et al., Biophys. J. 96 (2009) 5103-5111.
- [48] T. Savin, P.S. Doyle, Biophys. J. 88 (2005) 623-638.
- [49] H. Jayatilaka et al., Nat. Commun. 8 (2017) 15584.
- [50] P. Panorchan et al., Biophys. J. 91 (2006) 3499-3507.
- [51] J.L. Bays et al., J. Cell Biol. 205 (2014) 251-263.
- [52] M.J. Rosenbluth, W.A. Lam, D.A. Fletcher, Biophys. J. 90 (2006) 2994-3003.
- [53] M. Godin et al., Nat. Methods 7 (2010) 387-390.
- [54] B.G. Ricart et al., Biophys. J. 101 (2011) 2620–2628.

- [55] O.V. Sazonova et al., Biophys. J. 101 (2011) 622-630.
- [56] E.H. Zhou et al., PNAS 106 (2009) 10632-10637.
- [57] N.N. Pavlova et al., eLife 2 (2013) e00358.
- [58] D. Hanahan, R.A. Weinberg, Cell 144 (2011) 646–674.
- [59] C.Y. Li et al., J. Natl Cancer Inst. 92 (2000) 143-147.
- [60] H.E. Ryan, J. Lo, R.S. Johnson, EMBO J 17 (1998) 3005–3015.
- [61] Y. Aoka et al., Microvasc. Res. 64 (2002) 148-161.
- [62] B. Bellier et al., Vaccine 24 (2006) 2643-2655.
- [63] E.E. Kis, G. Winter, J. Myschik, Vaccine 30 (2012) 523–538.
- [64] Y. Tseng, T.P. Kole, D. Wirtz, Biophys. J. 83 (2002) 3162-3176.
- [65] T. Savin, P.T. Spicer, P.S. Doyle, Appl. Phys. Lett. 93 (2008).[66] M.H. Lee et al., Biophys. J. 102 (2012) 2731–2741.
- [67] B.N. Mason, Acta Biomater. 9 (2013) 4635–4644.

12

Please cite this article in press as: P.-H. Wu et al., Materials Today (2020), https://doi.org/10.1016/j.mattod.2020.03.021